EVALUATION OF ONE-DIMENSIONAL SEISMIC MODELS OF THE LUNAR INTERIOR

by

Yao Yao

A thesis submitted to the faculty of
The University of Utah
in partial fulfillment of the requirements of the degree of

Master of Science

Department of Geology and Geophysics

The University of Utah

August 2013

The University of Utah Graduate School

STATEMENT OF THESIS APPROVAL

The thesis of **Yao Yao**

has been approved by the following supervisory committee members:

Michael S. Thorne	, Chair	**6/11/2013** Date Approved
Keith Koper	, Member	**6/10/2013** Date Approved
Lowell Miyagi	, Member	**6/11/2013** Date Approved

and by **D.Kip Solomon** , Chair of

the Department of **Geology and Geophysics**

and by Donna M. White, Interim Dean of The Graduate School.

ABSTRACT

Continuous data from the Apollo Passive Seismic Experiment (PSE) were recorded from 1969 to 1977 at four sites on the lunar surface. These data have subsequently been used to generate nine unique one-dimensional seismic velocity models for the moon. In spite of the fact that these models were generated from the same data set, significant differences exist between them. We analyzed travel-time and waveform effects of these previously published seismic velocity models. In order to examine the predictive power of lunar seismic models currently in existence, we calculated the mean squared error between the predicted travel times of direct *P*- and *S*-waves for each and four published catalogs of seismic arrival time readings. The mean squared error of *P*-wave arrival times are smaller than that of *S*-wave arrival times for each model. Models typically fit artificial impacts, meteoroid impacts, and deep moonquakes better then shallow moonquakes. We found no systematic variation in travel times based on location of seismic station. We constructed a new model (referred to as YY13) of the lunar interior based on a weighted average of the other models with respect to how well they predict measured travel times. The YY13 model provides the least misfit based on all available lunar seismic data. In addition, we reprocessed a total of 85,466 moonquake traces recorded by the PSE and calculated the coda decay rate separately for shallow and deep events. Shallow events show relatively longer codas than deep events. We computed synthetic seismograms for

the YY13 mode and alternative versions of this with a varying thickness low velocity zone at the surface. By comparing synthetic seismograms with original data, it is challenging to reproduce the long seismic coda inherent in all lunar seismograms with a single low velocity or thin scattering layer as suggested by previous efforts.

To my parents Jun Yao and Shuang Hu.

TABLE OF CONTENTS

LIST OF TABLES

LIST OF FIGURES

ACKNOWLEDGMENTS

I would like to thank my supervisor, Dr. Michael Thorne, for his guidance, support, and encouragement throughout my study at the University of Utah. I am also grateful to Dr. Keith Koper and Dr. Lowell Miyagi for their helpful comments and support. I am thankful to Dr. Renee Weber and Dr. Nicholas Schmerr for their guidance in my work.

I gratefully acknowledge the University of Utah Center of High Performance Computing (CHPC) for computer resources and support. I was partially supported by NASA grant NNX11AH47G. Figures were drawn using the Generic Mapping Tools.

CHAPTER I

OVERVIEW

From 1969 to 1977, a network of four seismic stations was established and operated on the Moon as a part of the Apollo Lunar Surface Experiments Package (ALSEP) [*Latham et al.*, 1969]. As a part of ALSEP, the Passive Seismic Experiment (PSE) was designed to detect moonquakes in part to determine the structure of the Moon. The Apollo 11 seismometer was the first seismometer sent to the surface of the Moon and began streaming seismic data back to the Earth on July 16, 1969. However, it only operated for three weeks. Since then, another four seismometers were deployed with the Apollo 12, 14, 15, and 16 missions, transmitting lunar seismic data until 1977.

These stations deployed in the PSE were arranged roughly in a shape of a triangle (Figure 1) and located in different tectonic settings. Station 15 and 16 were separated by 1000 km with station 15 located mostly on mare material, while station 16 was in the central highland area. Stations 12 and 14 were located at the other corner of the triangle with a separation of 181 km between them. Station 12 was located on mare material but station 14 was located on a transitional region between mare and highland.

The moon was subsequently shown to be seismically active and over 12,000 moonquakes have been identified. Moonquakes can be classified into four categories:

artificial impacts, meteoroid impacts, shallow moonquakes, and deep moonquakes. Example seismograms from each type of event are shown in Figure 2. Artificial impacts were caused by crashing spacecraft sections onto the surface of the moon. The recordings from the artificial impacts helped to constrain the structure of the crust and upper mantle. The impact of meteoroids on the surface of the moon acted mostly as a compressional source of seismic wave energy, and thus *S*-wave arrivals are relatively hard to see for meteoroid impacts. Shallow moonquakes, also known as HFT (high-frequency-teleseismic) events, were much rarer events occurring between roughly 0 and 100 km in depth. What caused the shallow moonquakes is still not clear. A recent study suggested that the shallow moonquakes were triggered by objects like nuggets of strange quark matter coming from the outside of the solar system [*Frohlich and Nakamura*, 2006], but more shallow moonquake data are required to test this hypothesis. The last natural lunar seismic events were the deep moonquakes. They were the most numerous events and most of them could be grouped into spatially co-located clusters. In addition, the deep moonquakes occurred with distinct periodicities of 27 days, 206 days, and 6 years, which indicated that the deep moonquakes were triggered by the tidal stress caused by the gravitational field of the Earth. Among all of these moonquakes, roughly 7,355 of these events have been located, including 9 artificial impacts, 73 meteoroid impacts, and 28 shallow moonquakes [*Nakamura*, 2003](Figure 1). The majority of identified events (7,245) were deep moonquakes occurring in the depth range from 559 to 1419 km [*Nakamura*, 2005]

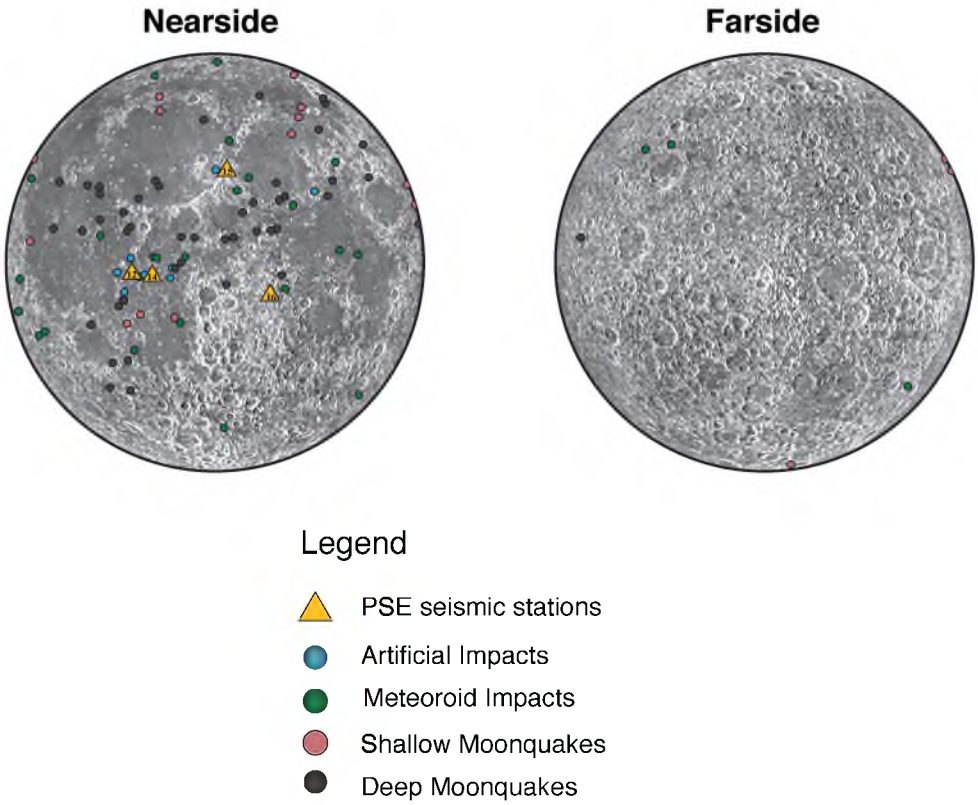

Figure 1. Locations of PSE seismic stations and four kinds of moonquakes. All PSE seismic stations were located on the nearside of the Moon, and only several events were detected on the farside of the Moon.

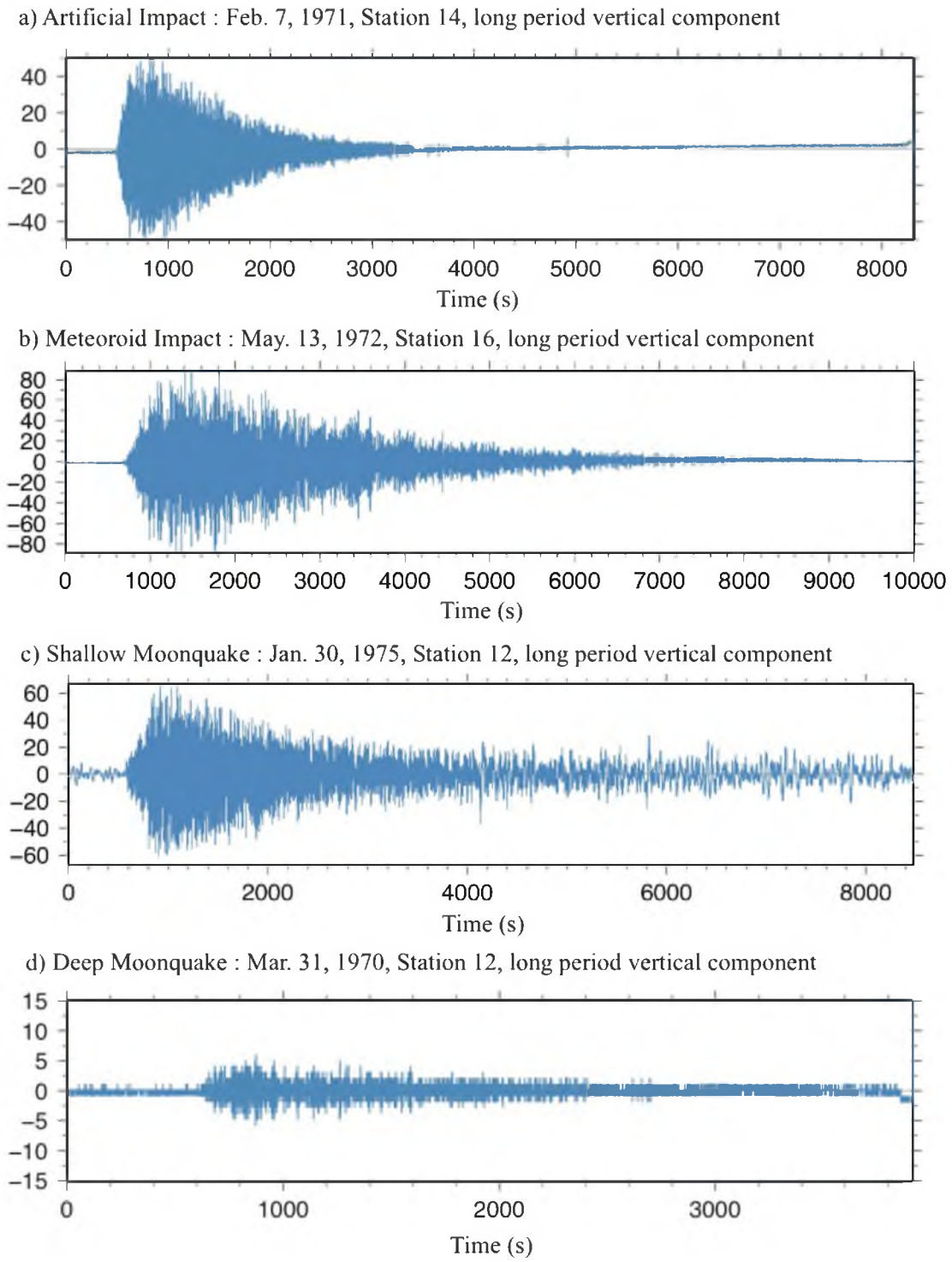

Figure 2. Examples of four kinds of moonquakes: a) Artificial Impacts, b) Meteoroid Impacts, c) Shallow Moonquakes, and d) Deep Moonquakes.

CHAPTER II

INTRODUCTION

From 1969 to 1977, a network of four seismic stations was established and operated on the Moon as a part of the Apollo Lunar Surface Experiments Package (ALSEP) [*Latham et al.*, 1969]. The instruments deployed consisted of a long-period (15 s resonant period) three-component seismometer collocated with a single short-period (1 s resonant period) vertical component seismometer. Subsequent analyses of data recorded in this experiment have identified over 12,000 moonquakes. Roughly 7,355 of these events have been located, including 9 artificial impacts, 73 meteoroid impacts, and 28 shallow moonquakes [*Nakamura*, 2003]. The majority of identified events (7,245) were deep moonquakes occurring in the depth range from 559 to 1419 km [*Nakamura*, 2005].

These data have been used to generate a suite of seismic velocity models for the lunar interior. Table 1 summarizes the different modeling techniques and Figure 3 shows a comparison of *P*- and *S*-wave velocities for these models. The majority of these models are characterized by a low velocity layer (roughly 1 to 2 km thick) with extremely reduced wave speeds (V_P and V_S roughly 1.0 and 0.5 km/s, respectively) at the surface representing the lunar regolith. This regolith layer overlies the crust that varies in thickness between the models from 28 to 60 km. The crustal *P*-wave velocity varies from

5.5 to 7.0 km/s and the *S*-wave velocity varies from 2.1 to 4.4 km/s. Beneath the crust, the lunar mantle is nearly homogenous with an average *P*-wave velocity of 7.7 km/s and *S*-wave velocity of 4.4 km/s. Because seismic recordings were restricted to the near-side of the Moon and only a handful of far-side moonquakes were detected, the seismic velocity structure of the Moon is typically not determined to depths greater than roughly 1000 km. Nevertheless, two recent studies reported observations of core reflected waves. By detecting core reflected *S*-waves, Garcia *et al.* [2011] estimated a core radius of 380 ± 140 km. Weber *et al.* [2011] proposed the presence of a solid inner core with a radius of 240 km and a 110 km thick fluid outer core, covered by a partially molten boundary layer with the thickness of approximately 150 km by searching for core reflected and converted seismic energy. Their study indicated a *P*-wave velocity inside the solid core of 4.32 km/s and *S*-wave velocity of 2.25 km/s. Despite these two recent observations, much uncertainty still exists in the size and composition of the lunar core.

Despite the overall similarities in the wave speed models, inspection of Figure 1 shows that significant differences exist between these models (refer to Table 1 for model reference and the model naming code). Namely, one model (GG11) maintains a subtle velocity increase throughout the entire mantle, whereas other models include discontinuous velocity structure. For example, model N83a has a discontinuous low velocity layer between depths of 270 and 500 km. Possible discontinuity structure has been used to speculate on compositional structure within the Moon and may indicate the presence of an early magma ocean [*Lognonné and Johnson*, 2007]. One model (KM02) has an average velocity structure that is significantly larger (e.g., V_P in model KM02 is 39% larger than for model N83a at 800 km depth) than all other models. Determination

of the actual seismic velocity structure, size, and composition of the core, and whether or not discontinuous velocity changes exist in the Moon's mantle is crucial to understanding its formation and evolution.

Future missions to the Moon will seek to gain better constraints on its interior structure and composition. Significant challenges exist in seismically examining the lunar interior due to strong scattering of seismic energy. Hence, planning for such missions will be aided by the ability to predict lunar ground motions through computation of synthetic seismograms and testing different seismic array geometries. Thus, we are motivated to assess the predictive power of lunar seismic models currently in existence. In this paper, we examine the collection of previously published lunar seismic velocity models comparing with predicted travel-times of direct *P*- and *S*-waves for each model to four published catalogs of seismic arrival time readings [*Goins*, 1978; *Lognonnè et al.*, 2003; *Nakamura*, 1983; 2005]. We construct a new model of the lunar interior based on a weighted average of the other models with respect to how well they predict measured travel-times. In addition, we reprocess the Apollo data and compute coda decay rates as a basis for comparing the prediction power of synthetic models.

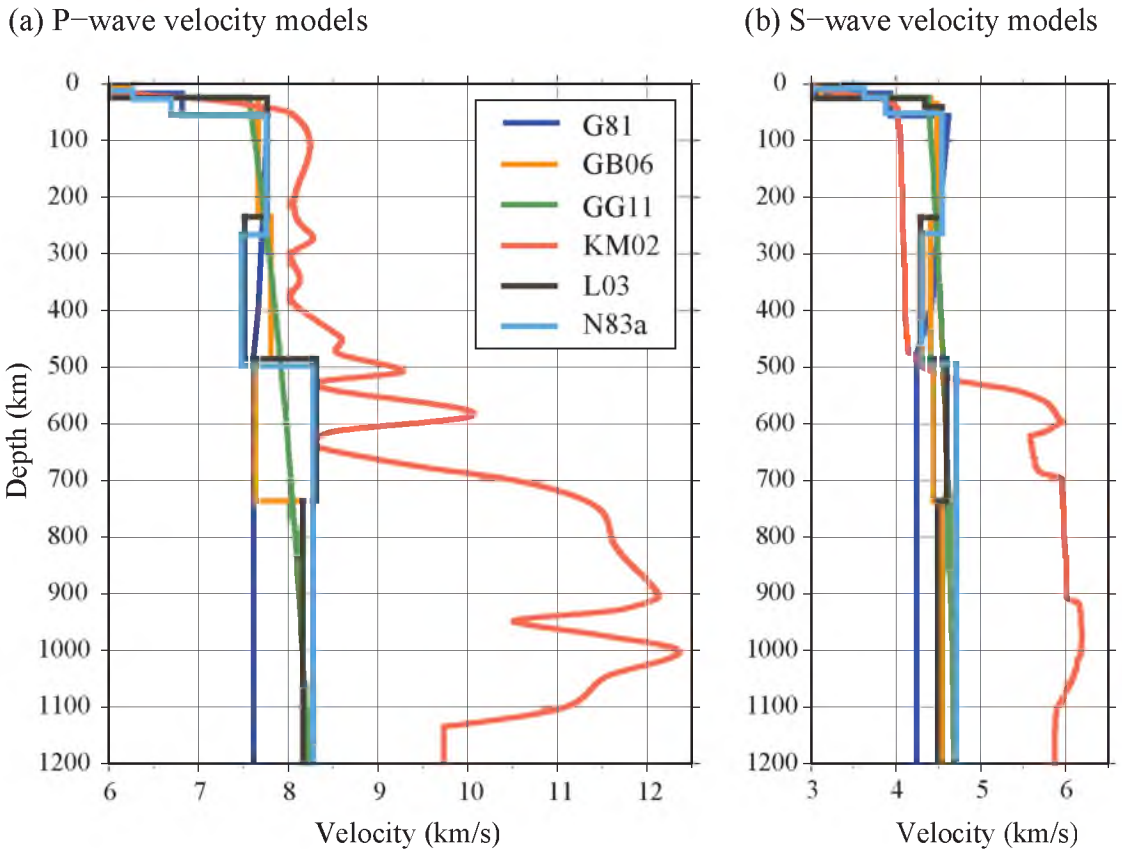

Figure 3. Seismic velocity models for the crust and mantle of the Moon. (a) *P*-wave velocity models as a function of depth. Model codes are listed in Table 1. (b) *S*-wave velocity models.

Table 1. 1D Lunar Models Analyzed in This Study

Model Code	Travel Time Picks	Model Inputs	Additional Constraints And Notes	Model Reference
G81	Individual picks	228 direct P- and S-wave travel-times.	A crust model by Cooper *et al.* [1974] Indirect seismic wave arrival times Direct P- and S- wave amplitude	[*Goins et al.*, 1981]
GB06	[*Lognonnè et al.*, 2003]	319 direct P- and S-wave travel-times.		[*Gagnepain-Beyneix et al.*, 2006]
GG11	[*Lognonnè et al.*, 2003]	343 direct P- and S-wave travel-times.	Lunar mass Polar moment of inertia Love numbers	[*Garcia et al.*, 2011]
KM02	[*Nakamura*, 1983]	428 direct P- and S-wave travel-times.		[*Khan and Mosegaard*, 2002]
L03	Individual picks	316 direct P- and S-wave travel-times.	Lunar Prospector gravity data	[*Lognonnè et al.*, 2003]
N76	Individual picks	Shear wave amplitude for 35 events. S-P travel-time intervals for 45 events.		[*Nakamura et al.*, 1976]
N83a	Individual picks	438 direct P- and S-wave travel-times.		[*Nakamura*, 1983]
N83b	Individual picks	438 direct P- and S-wave travel-times.	Same data as N83a, but used functional velocity increase from 270 to 500 km depths instead of a single low velocity layer	[*Nakamura*, 1983]
W11	Individual picks	62 direct S-wave travel-times.	L03 model for crust and mantle Love number obtained from Lunar Laser Ranging	[*Weber et al.*, 2011]

CHAPTER III

TRAVEL TIME COMPARISON

The majority of the lunar models are provided as one-dimensinal radial models of seismic velocity as a function of depth (models N76, G81, N83, W11, GG11). Model N83 is given in two forms. The first form (which we refer to as N83a) has a discontinuous velocity decrease from 270-500 km depths. However, Nakamura [1983] noted that this discontinuous decrease may produce a shadow zone which was unobserved in data. Hence, the second form of the model (here referred to as N83b) is a functional form with continuously decreasing velocities in this depth range. The remainder of the models (models KM02, L03, and GB06) reports the probability of a given seismic velocity with depth. For each of these models, we use the seismic velocity with the maximum assigned probability. Details on the models we used are provided in the auxiliary material.

We took measured *P*- and *S*-wave arrival times and *S*-*P* differential travel times from the catalogs of Goins [1978], Lognonnè *et al.* [2003], and Nakamura [1983; 2005]. Table 2 summarizes the number of measurements in each catalog based on event type. We computed predicted travel times for each model (Table 1) using the TauP Toolkit [*Crotwell et al.*, 1999]. We calculated the mean squared errors between predicted and

observed *P*- and *S*-wave travel times as well as *S*-*P* differential travel times for each model and each event in these four catalogs. The results are summarized in Figure 4 where we have separately calculated the error based on event type. Model YY13 is a weighted average model that we derive in this paper and will discuss in the next section. In general, the mean squared error of *P*-wave arrival times is smaller than that of *S*-waves for each model. Lunar seismograms are characterized by long coda obscuring *S*-wave onsets, thus making accurate *S*-wave arrival time picks more difficult. Moreover, models typically fit artificial, meteoroid impacts and deep moonquakes better than shallow moonquakes. This is likely due to the uncertainty in source depth for shallow moonquakes. Since most of the shallow moonquakes are outside of the array, they are challenging to locate.

Models GG11, L03, N83a, and W11 all predicted the *P*-wave arrival times comparably well. These models also explained each of the different event types almost equally as well. Models G81, N76, and N83b performed slightly worse. Model GB06 has a relatively larger *P*- and *S*-wave velocity on the surface, so the mean squared error of artificial impacts for GB06 was 25 which is comparable to the error for artificial impact measurements for the other models. The large *P*-wave velocities in model KM02 manifested in much larger error in the *P*-wave predictions. Nevertheless, model KM02 has significant error for the other event types. The maximum error is 38 for deep moonquake events. Overall, models GG11, L03, and N83a predicted the P-wave arrival times the best.

The average mean squared error of *S*-wave arrival times is 55 percent larger than that for *P*-wave arrival times For artificial and meteoroid impacts, most of the seismic energy

is compressional, thus leading to lower amplitude of *S*-wave arrivials and making *S*-wave travel-time less accurate for artificial and meteoroid impacts. Shallow moonquakes show distinctive *S*-wave arrivals, but the depths of the shallow moonquakes in the travel-time catalogs are fixed to zero since most of the shallow moonquakes are located outside of the array, making depth determination challenging. Therefore, the high error of *S*-wave arrival times for shallow moonquakes is likely due to the source depth uncertainty. The deep moonquakes are energetically much weaker than shallow events and as a result display small signal amplitudes. For these deep events, the *P*-wave arrivals are often not well-observed but clear S-wave arrivals are common. However, a higher error of *S*-wave arrival times than *P*-wave arrival times can still be observed. This may be related to uncertainty in depth of the deep moonquake clusters and relatively low signal-to-noise ratio of deep moonquakes There is also more scatter between different event types in the *S*-wave data. Models G81, GG11, L03, and N83a predicted *S*-wave arrival times with average mean squared error less than 20 for all event types. Models KM02, N76, N83b, and W11 have the largest error.

For *S*-*P* differential travel times, the average mean squared error of all types of moonquakes is reduced by 26 percent compared to *S*-wave travel times. The average mean squared error for both artificial impacts and shallow moonquakes is reduced by more than 40 percent compared to *S*-wave travel times. In general, KM02 and N76 had the largest error, but the mean squared error for all other models is nearly identical.

We also calculated the mean square error for the four Apollo stations seperately in order to assess if there are any systematic variations based on local site effects. For *P*-wave travel times, there is no significant difference between the four stations. However,

S-wave travel times from station 16 has a slightly higher error than other stations. Since station 16 has the most "ringing" character of all the stations [*Goins*, 1978], the long coda in the records of station 16 obscures *S*-wave onsets, which introduces more error in making accurate arrival time picks. Despite the increased error at station 16, there is no systematic bias based on location of seismic instruments.

In general, the mean squared error of *P*-wave arrival times are smaller than that of *S*-wave arrival times for each model. Models typically fit artificial impacts, meteoroid impacts, and deep moonquakes better then shallow moonquakes. Models GG11, L03, N83b, and W11 provide the best overall fit to the complete set of travel-times used. We found no systematic variation in travel-times based on seismic station location.

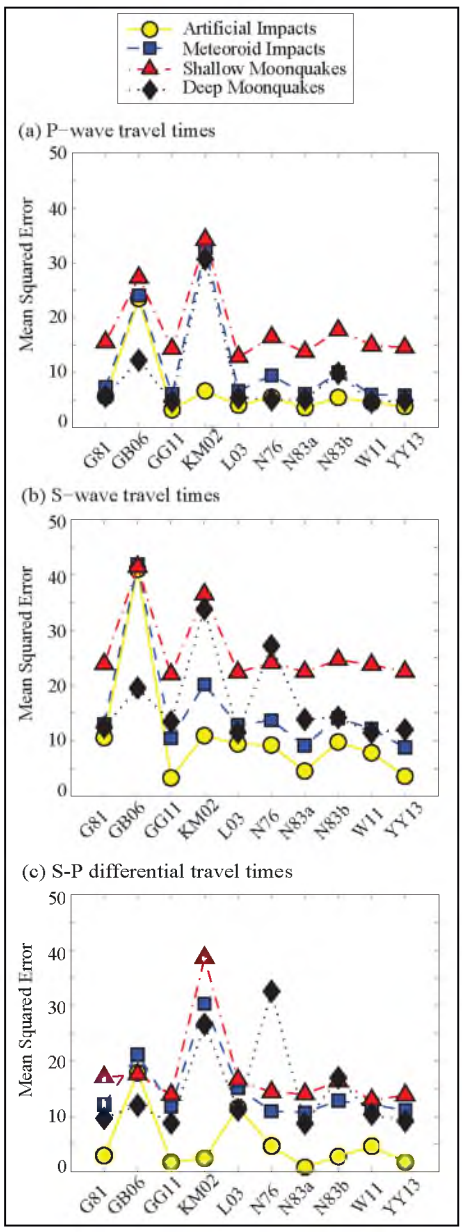

Figure 4. Mean squared errors between travel time readings and predicted travel times for all models. (a) Direct *P*-wave travel times. (b) Direct *S*-wave travel times. (c) *S-P* differential travel times. Results in each panel are grouped by event type: gold circles – artificial impacts, blue squares – meteoroid impact; red triangles – shallow moonquakes; black diamonds – deep moonquakes. Model codes along the x-axis are given in Table 1.

Table 2. Number of Measurements in Moonquake Catalogs*

	P-wave		*S*-wave		*S-P* times		
Artificial Impacts	L2003 15	N1983 12	L2003 2		L2003 2		
Meteoroid Impacts	L2003 68	G1978 27	L2003 18	G1978 10	L2003 16		G1978 10
Shallow Moonquakes	L2003 24	G1978 27	L2003 19	G1978 19	L2003 16		G1978 20
Deep Moonquakes	L2003 71	G1978 50	L2003 90	G1978 90	L2003 66	N2005 117	G1978 48

*L2003: [*Lognonnè et al.*, 2003], N2005: [*Nakamura*, 2005], N1983: [*Nakamura*, 1983], G1978: [*Goins*, 1978]

CHAPTER IV

WEIGHTED AVERAGE MODEL

A total of nine lunar seismic velocity models have been published. These models differ in the data they used and method in which they were derived (Table 1), and in the previous section, we have evaluated their ability to predict travel times. Here we generate a weighted average seismic velocity model in order to take the best features of each model.

To generate this model, we converted each of the previously published models into a stack of discrete 5 km thick layers. Weights were assigned based on the mean squared error calculated in the previous section: the larger the error, the smaller the weight assigned to the weighted average velocity model. Therefore, we put more weight on the models that provide better predictions of Lunar seismic velocity structure than other models. The relationship between the *P*- and *S*-wave velocities in the weighted average model and in nine of other models can be expressed as

$$V_P = \sum_{i=1}^{9} \omega_i V_{Pi} \qquad (1)$$

$$V_S = \sum_{i=1}^{9} \omega_i V_{Si} \qquad (2)$$

where V_{Pi} and V_{Si} are P- and S-wave velocities in this layer for the ith model, ω_i is the weight for the ith model, and V_P and V_S are the weighted average P- and S-wave velocities in this layer. We calculated P- and S-wave velocities to 1500 km depth. We adopted the inner-core structure of model W11. A comparison between the P- and S-wave velocity structure of the weighted average model (hereafter referred to as Model YY13) and the models used to construct it is shown in Figure 5, and the actual values of model YY13 are provided in Table 3.

We calculated the mean squared error of YY13. This model shows that the average mean squared error across all event types and travel-time types (P-, S-wave and S-P travel-times) is the smallest. Although YY13 fails to provide the smallest mean squared error in some individual data types (e.g., shallow moonquakes P-wave travel-time), it does a better job than other models if we consider all kinds of moonquakes in all P-wave, S-wave, and S-P differential travel-time readings (Figure 4). It has the fourth smallest, smallest, and second smallest mean squared error for P-wave, S-wave, and S-P differential travel-time readings. This model provides the smallest mean squared error for meteoroid impacts and deep moonquakes, and the third third smallest mean squared error for artificial impacts and shallow moonquakes. Moreover, since this model is a combination of all other models, it avoids bias caused by using a different method of inversion and data types. Although YY13 has its own bias since it combines all models without redoing the velocity inversion, it is a model with the least misfit based on all

available Lunar seismic data. We use YY13 as a starting point for synthetic waveform analysis described in Section 5.

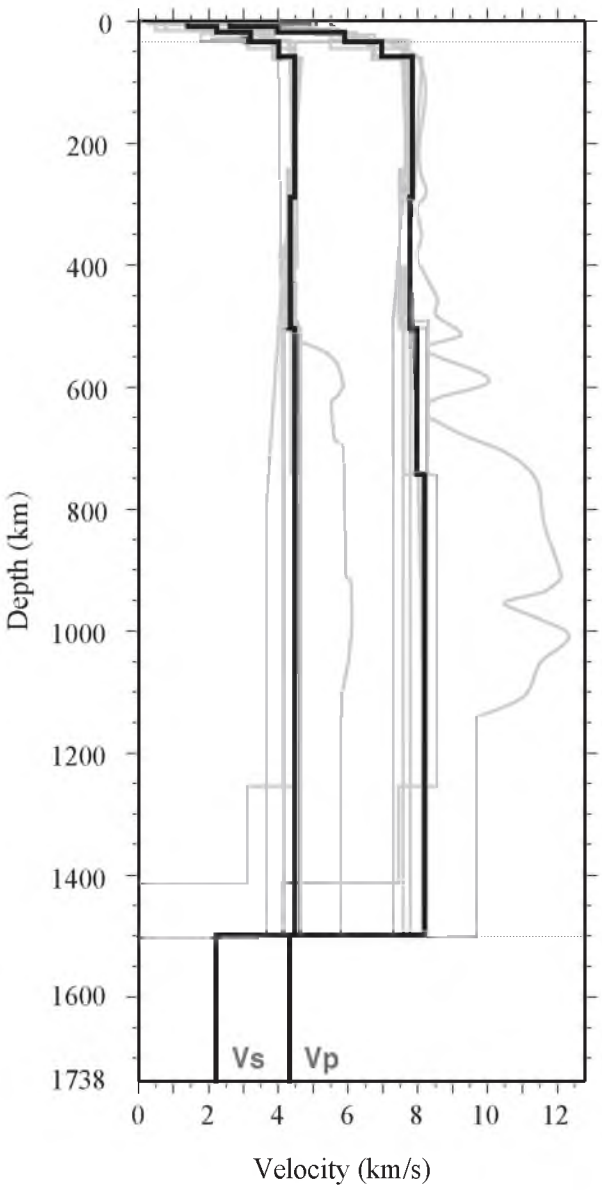

Figure 5. Weighted average seismic velocity model compared with Model G81, GB06, GG11, KM02, L03, N76, N83a, N83b, and W11(grey lines). The inner core structure of this model was simply adopted from W11 model. Dashed lines divided the structure by crust, mantle, and core approximately. Solid black lines represents *S*- and *P*-wave velocity structure.

Table 3. Weighted average model*

	Depth (km)	V_P (km/s)	V_S (km/s)
Crust	0	2.65	1.46
	0.4	3.94	2.21
	5	3.97	2.27
	15	5.85	3.22
	30	6.89	4.01
Mantle	55	7.75	4.46
	285	7.68	4.33
	500	7.87	4.46
	740	8.09	4.46
Core	1495	4.32	2.25
	1738		

* Seismic velocities in the inner-core are from the work of Weber *et al.* [2011]

CHAPTER V

CODA DECAY RATES

Seismograms recorded in the Apollo mission present extended rise times and long, reverberating codas (Figure 6). These characteristics of lunar seismograms are due to strong scattering effects [*Berckhemer*, 1970]. Latham *et al.* [1971] suggested that scattering in a layer with finite thickness near the surface can explain the observed data. Using seismograms filtered around 0.45 Hz and 14 km at 1 Hz, Dainty *et al.* [1974] stated a scattering layer with an average thickness of 25 km was reasonable based on the relationship between the rise-time of seismic energy envelope and epicentral distance at certain frequency bands. Much of the lunar scattering may be due to a thin surficial layer; however, the full depth extent and scale of lunar seismic scatterers is still unknown. .

A total of 3387 moonquake events including 9 artificial impacts, 19 meteoroid impacts, 8 shallow moonquakes, and 3,351 deep moonquakes were recorded by Apollo missions at stations 12, 14, 15, and 16 between 1969 and 1977. Each station recorded 4 traces including three long period components (lpx, lpy, and lpz component) and one short period component (spz component). We considered all 3387 moonquake events which included 85466 traces as our original data set. Our data processing steps consisted of (1) we used a despiking filter to remove high-amplitude thermal spikes, and (2) we

applied a band pass filter from 0.25 Hz to 3.3126 Hz [see e.g., *Bulow et al.*, 2005]. In order to examine the seismic coda waves, we next calculated the envelope of the seismic trace using Hilbert transform. As not all stations worked properly when a moonquake occurred, some traces just recorded random spikes or partial seismograms without the beginning or the ending of the event. Therefore, in order to get rid of some unreasonable traces which can not be used to study the coda decay rate, we manually went through each trace and discarded these traces. We also calculated the signal-to-noise ratio (SNR) of each trace by dividing the peak amplitude by the average noise amplitude, where the average noise was determined by calculating the absolute average amplitude inside a 701 point sliding window which moved from the beginning of the seismogram until the time point when the event began. We selected the highest quality data by retaining only those records with a SNR greater than 5. After this initial quality control step, we retained a total of 951 traces including 275 lpx traces, 448 lpy traces, 95 lpz traces, and 143 spz traces. We next calculated the moving average of the envelope with a window of 701 points (approximately 2 min) in order to smooth the envelope. We determined a beginning time for when the seismic energy starts to emerge from background noise by examining the slope of the smoothed envelope function. In particular, we used a 501 point sliding window and calculated the average slope within this window. If the average slope inside the window was larger than 0.03, we assigned the first point of this window as the begin time (see Figure 6). The time where the smoothed envelope reached its maximum amplitude was also picked for each trace in order to determine where the coda starts to decay. As the coda decay rate is exponential, we converted the amplitude envelope to log scale in order to fit a straight line to the coda. The slope of the best-fit

line was used as the coda decay rate for each trace. Figure 6 shows an example of how the coda decay function fits (not in log-space) the moving average of the envelope. We classified moonquakes by shallow events including artificial impacts, meteoroid impacts, and shallow moonquakes that occurred on or near the surface, and deep events that were defined as deep moonquakes. A total of 174 shallow traces and 787 deep traces were selected to calculate coda decay rate. We shifted the traces by the begin time and stacked them in 10° epicentral distance bins (Figure 7a). Figure 7 shows the average behavior of the lunar seismic coda for both shallow and deep events as a function of epicentral distance. From this figure, we can see that in general, the coda decays slower for shallow events than for deep events. We also calculated the average coda decay rate per 10° bin (Figure 7b). There is a slight increase in decay rate for both types of events. In addition, the absolute values of decay rate for shallow events are smaller than deep events in the most cases, which was consistent with the conclusion we got from Figure 5a.

In general, shallow events have relatively longer codas than deep events and the codas for deep events decay faster than shallow events. As the epicentral distance increases, the coda becomes longer for both shallow and deep events. For example, at a distance of 5°, the coda returns back to average noise levels around 2400 s for deep events and 3000 s for shallow events. Whereas at a distance of 85°, the coda returns back to average noise levels at 3200 s for deep events and 4000 s for shallow events.

Previous efforts have described the generation of lunar coda by the scattering of surface waves [*Berckhemer*, 1970], surface scattering of body waves [*Gold and Soter*, 1970], and scattering of seismic energy in a surficial layer [*G Latham et al.*, 1971]. Dainty *et al.* [1974] used an analog method of simulating seismic scattering in which

acoustic waves were propagated across a metal plate with 0.06-inch wide and 1-inch long grooves milled half-way through the plate as the surficial scattering layer overlying a homogeneous medium. He generated a pulse source as the input of the model. The output of his model provided similarity with the observed scattering properties of Apollo data; however, actual verification by simulating seismograms has yet to be achieved. Comparison between synthetic seismograms and original seismograms for both shallow events and deep events is needed to determine the details on the origins of the lunar scattering.

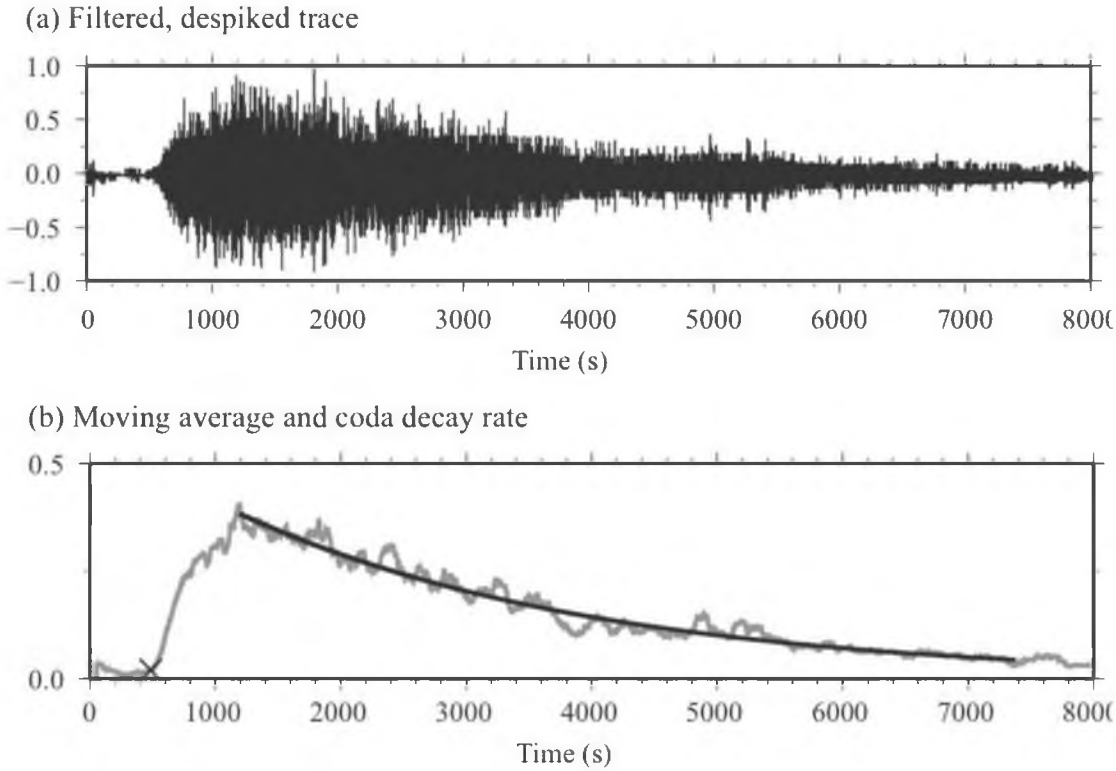

Figure 6. Examples of a) filtered, despiked moonquake displacement seismogram and b) moving average of displacement envelope and coda decay fitting line. Light grey line is the moving average of the envelope and black line is the fitting line used to calculate coda decay rate. The seismogram shown in this figure is a horizontal component of a deep moonquake which occurred at 13:17 on 17 July 1974 at station 15.

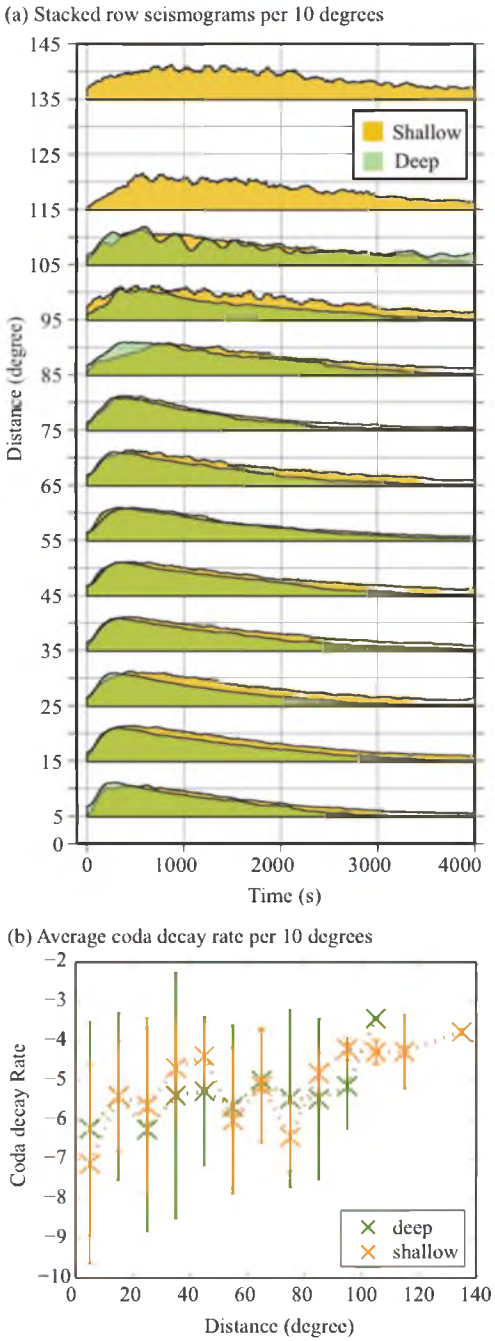

Figure 7. Comparison between shallow and deep events. (a) Traces were shifted by the begin time we picked and stacked per 10 degrees separately for shallow events (yellow) and deep events (green). (b) Average coda decay rate was calculated every 10 degrees. In general, shallow events have larger coda decay rate than deep events.

CHAPTER VI

SYNTHETIC SEISMOGRAMS

We computed synthetic seismograms using the Green's Function of the Earth by Minor Integration (GEMINI) method [*Friederich and Dalkolmo*, 1995]. We have modified the code to work on lunar models. This code computes the full wavefield for 1-D radial models and with dominant periods down to 10 s. Although the recorded lunar data typically have dominant periods of about 1 s, our goal was to determine the primary differences in synthetics between these models and not necessarily try to model individual events.

Models of the lunar interior generally provide *P*- and *S*-wave velocities as a function of depth, but not all models provide density structure and/or quality factors (Q) which are needed to generate synthetic seismograms. Several studies have published density models [*Bills and Ferrari*, 1977; *Garcia et al.*, 2011; *Hood and Jones*, 1987; *Kuskov*, 1997; *Kuskov and Kronrod*, 1998; *Toksöz et al.*, 1974; *Weber et al.*, 2011], but the variation in these models is not large. Hence, we used an average three-layer density model characterized by: (1) crust: $\rho = 2.95$ g/cm^3; mantle: $\rho = 3.41$ g/cm^3; and core: $\rho = 6.51$ g/cm^3. The effect of these densities on our synthetic seismograms does not affect

the travel times but primarily effects the impedance contrast at the base of the crust. Details on the construction of our density model were provided in the auxiliary material.

We also constructed an average Q model based on previous attenuation models [*Goins et al.*, 1981; *Nakamura et al.*, 1982; *Toksöz et al.*, 1974]. This model was also a three-layer model where we used the same Q for both Q_S and Q_P: (1) crust: Q = 6000, (2) mantle: Q = 1500, and (3) core: Q = 500. Details on the construction of our Q model were also provided in the auxiliary material.

We used the YY13 model that we generated in Section 3 as the input 1-D radial model in GEMINI, together with average density model and average Q factor model. The depth of the event was set as 0 km for shallow event and 700 km for deep event. We stacked synthetic seismograms into 10° epicentral distance bins in the same way as we did the data. Figure 8 shows the comparison between shallow event (yellow) and deep event (green). Compared with the stack of Apollo seismograms (Figure 5a), the synthetic seismograms have relatively shorter rise-time of the amplitude envelope and extremely shorter coda decay time. In addition, the difference of the coda decay rate between shallow events and deep events is unnoticeable in synthetic stack seismograms. The unconsidered effects of seismic scattering structure in generating synthetic seismograms can explain these phenomena. Furthermore, from the comparison between Apollo program seismograms and synthetic seismograms, we can clearly see the significant importance of the presence of the scattering layer in affecting the appearance of lunar seismograms.

We performed another test to determine how the seismograms change if we change the low velocity layer at the surface from 0.4 km thick to 5 km thick (Table 3). The entire

surface of the Moon is covered by the "regolith" whose thickness varies from 5 m at lunar mare to 10 m at highland surface [*Schmitt et al.*, 1991]. The velocities of *P*- and *S*-wave are slightly increasing beneath the regolith layer as the composition changes from the regolith to ejecta and structurally distributed crust. Here we extend the low velocity layer in YY13 model to 5 km depth with *P*-wave velocity as 2.65 km/s and *S*-wave velocity as 1.46 km/s. This alternate model was also used to generate synthetic seismograms and we followed the processing steps discussed above for postprocessing these traces. Finally, a stack of seismograms per 10 degrees was made (Figure 9). Compared to the original YY13 model (Figure 8), this alternate model (Figure 9) has a significant longer coda decay time and a smaller coda decay rate, which is more similar to the stack of seismograms from the Apollo data set (Figure 7). However, the rise-time of these two models does not show significant difference in waveform character. By extending the low velocity layer, we made a rough estimation of what the stack seismograms should look like when we add seismic scattering structure to the YY13 model. However, the low velocity on the surface extends the coda decay rate but still under predicts the decay time by roughly 2500s, but the low velocity layer does not significantly change the rise time of the traces. Further efforts should focus on embedding scattering structure in the upper most layers of the lunar crust.

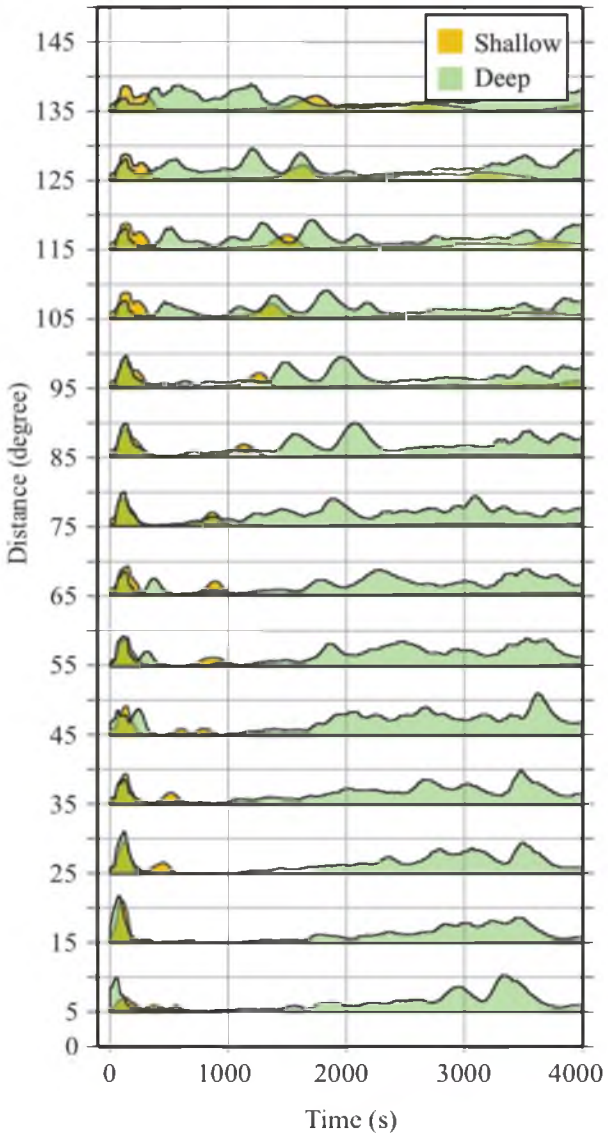

Figure 8. Synthetic seismograms generated by GEMINI for shallow event (depth = 0 km, yellow) and deep event (depth = 700 km, green) based on YY13 model were shifted by start time we picked and stacked every 10 degrees. The significant differences between synthetic stack seismograms and Apollo program stack seismograms mainly caused by scattering structure on the surface.

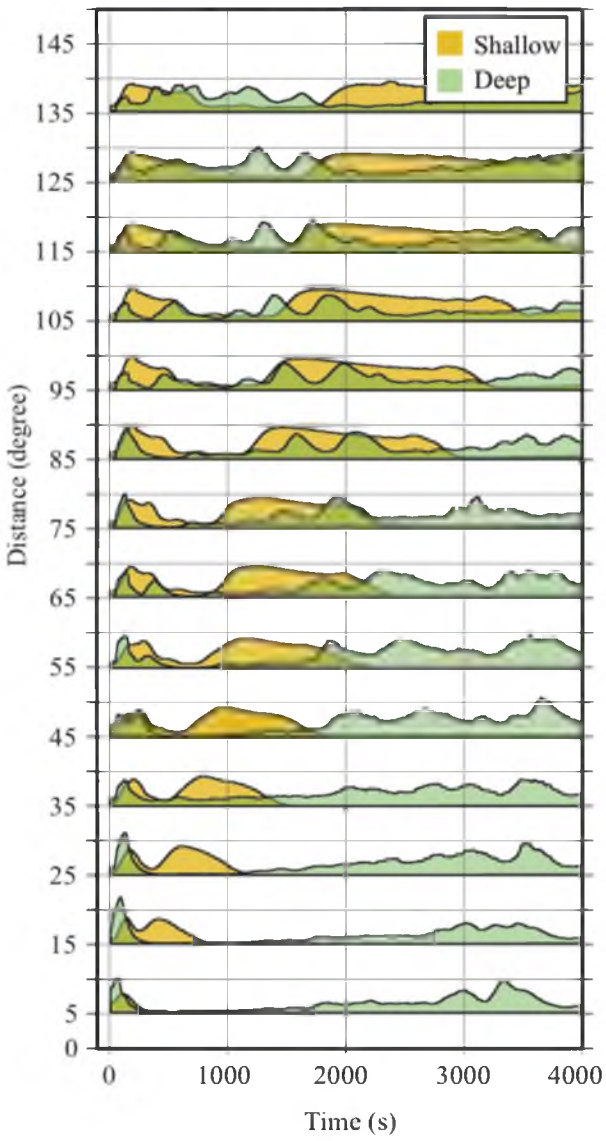

Figure 9. Synthetic seismograms generated by GEMINI for shallow event (depth = 0 km, yellow) and deep event (depth = 700 km, green) based on an alternative version of YY13 model with 5 km thickness of low velocity layer. Traces were shifted by start time we picked and stacked every 10 degrees.

CHAPTER VII

DISCUSSION AND CONCLUSION

In addition to the coda decay rate, we also calculated the rise-time of both shallow and deep events. We defined the rise-time as the time interval between the time when the amplitude of the seismogram starts to increase and the time of the maximum amplitude. Figure 10 shows the comparison of rise-time between shallow events and deep events. In general, the rise-time of shallow events was almost twice as long as the rise-time for deep events at almost all distances. The rise-time also slowly increases with increasing distance. Shallow events begin in the surficial scattering layer and much of the energy is thus scattered at the onset. This energy also passes through this layer a second time as it emerges near the receiver; however, deep events only travel through the scattering layer once. Ultimately, we expect shallow events to reach the maximum amplitude after a longer time. However, we must consider the different ray path between shallow events and deep events. At the same offset distance between the source and receiver, the ray path of deep events is much shorter than that of shallow events. If the lunar mantle is nearly homogeneous, the difference in the length of the ray path may not be enough to lead to a significant increase in the rise time. However, whether there is a lack of scattering structure in the lunar mantle is still questionable. If scattering exists in the

lunar mantle, the longer ray path of shallow events can also lead to more scattering of the seismic energy, which means the shallow events will take a longer time to reach the peak amplitude. Therefore, it is difficult to determine whether the longer rise-time of shallow events is caused by the double crossing of a shallow scattering layer or the longer ray path. It is possible that both of these factors play an important role in extending the rise time of shallow events. Moreover, the separation between *P*-wave arrival and *S-wave* arrival also affects the length of the rise time. Since *P*-wave propagates faster than *S*-wave, the longer the ray path is, the longer the separation between *P*-wave arrival and *S*-wave arrival is. Therefore, the shallow events have a longer ray path that leads to a longer separation between *P*-wave and *S*-wave arrival, and then the rise time of shallow events is longer. In order to remove this factor, we need to pick the *P*-wave and *S*-wave arrival and calculate the *S-P* differential travel time, then subtract the *S-P* differential travel time from the rise time in order to remove the effect of the separation between *P*-wave and *S*-wave.

We calculated the coda decay rates for short period data as well. However, the coda decay rates calculated based on short period data were much more scattered than that based on long period data. For example, the coda decay rate of long period data varied from -10 to -4 and had an average value of -7 (Figure 7b). However, for short period data, the coda decay rate varied from -50 to -10 with an average value of -30. We also noticed that for short period data, deep events were more scattered (coda decay rate varies from -50 to -10) than shallow events (coda decay rate varies from -35 to -12). Because the short period components of the seismometers recorded most of the high

frequency seismic events and most of them were shallow events, they may not be that accurate in recording deep events.

Overall, we generated a weighted average model based on the calculation of mean squared error between predict travel times and observed travel times for a total of nine models. This new model of the lunar interior, the YY13 model, predicts the observed travel times for the sum of all classes of moonquakes better than previously constructed models. We reprocessed the Apollo seismic data revealing the relationship between the coda decay rates and the location of the seismic events. In general, shallow events have relatively longer codas than deep events and the codas for deep events decay faster than shallow events. As the epicentral distance increases, the coda becomes longer for both shallow and deep events. We used synthetic analysis to compare the waveforms between the stack of observed lunar seismograms and the stack of synthetic seismograms based on weighted average model demonstrating that simple one-dimensional models are not capable of predicting the long coda decay rates inherent in lunar seismograms. Future efforts must focus on inclusion of realistic scattering models in synthesizing waveforms. However, the computational cost of adding realistic scattering will be a significant challenge, especially if multiple scattering or a fully three-dimensional lunar model is required.

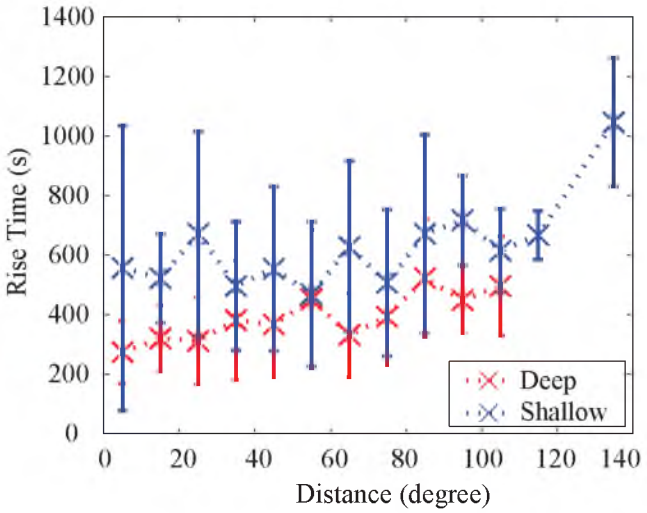

Figure 10. Average rise time was calculated every 10 degrees. In general, shallow events have greater rise time than deep events.

APPENDIX

SUPPLEMENTARY MATERIALS

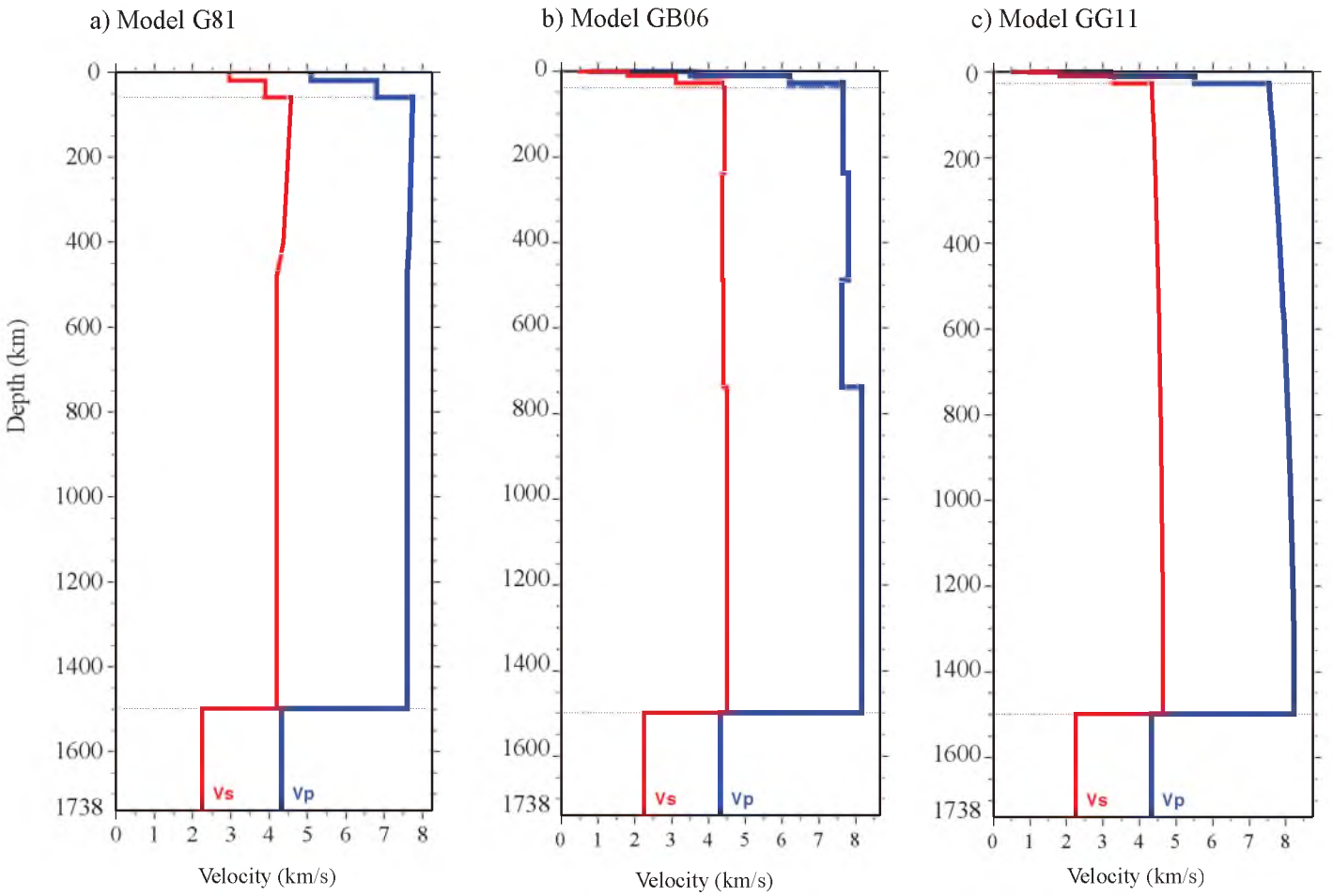

Figure 11. Shear wave and *P*-wave velocity structure for Model G81, GB06, and GG11. Core structure was adapted from Weber's work [*Weber et al.*, 2011].

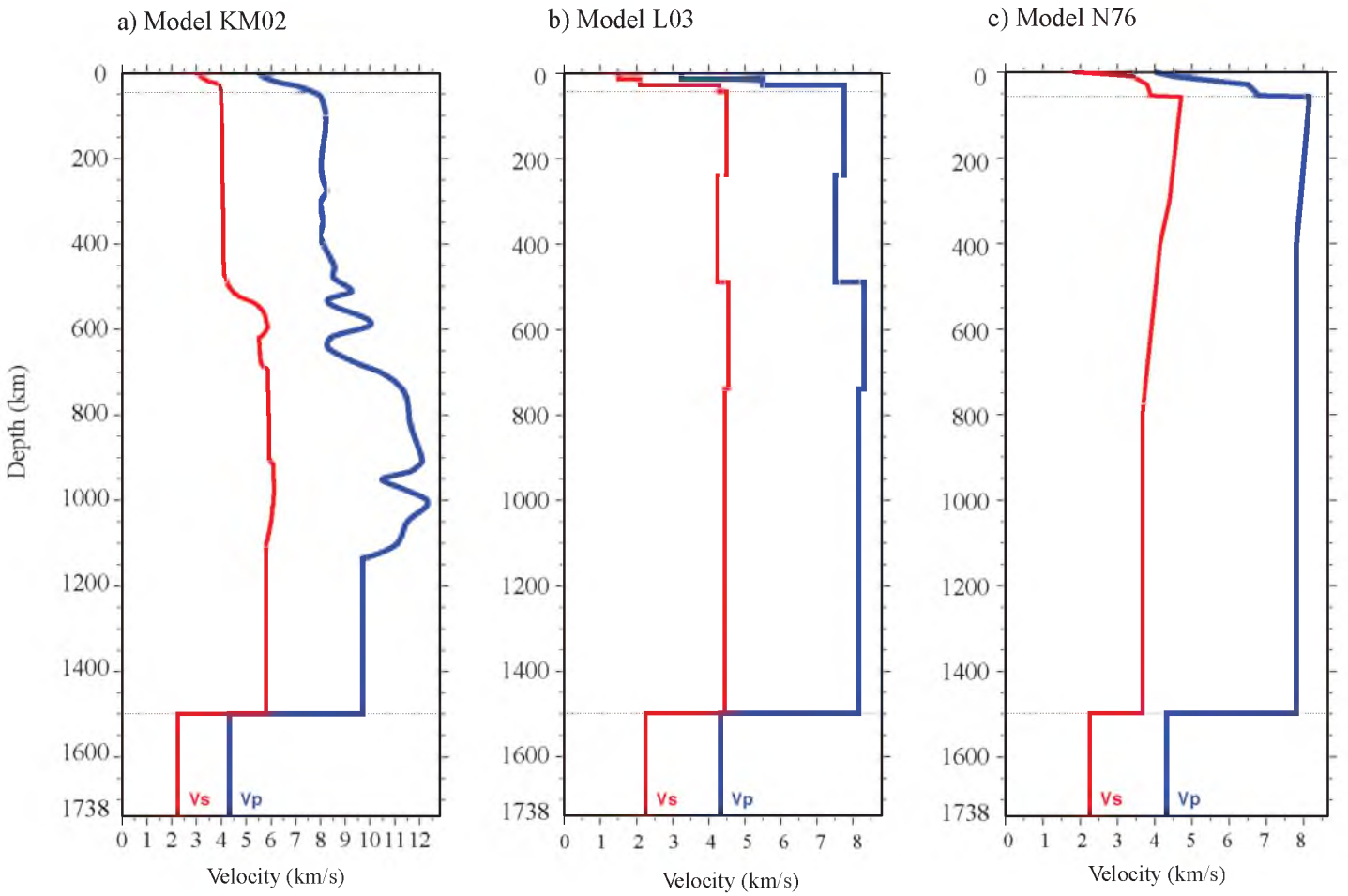

Figure 12. Shear wave and *P*- wave velocity structure for Model KM02, L03, and N76. Core structure was adapted from Weber's work [*Weber et al.*, 2011].

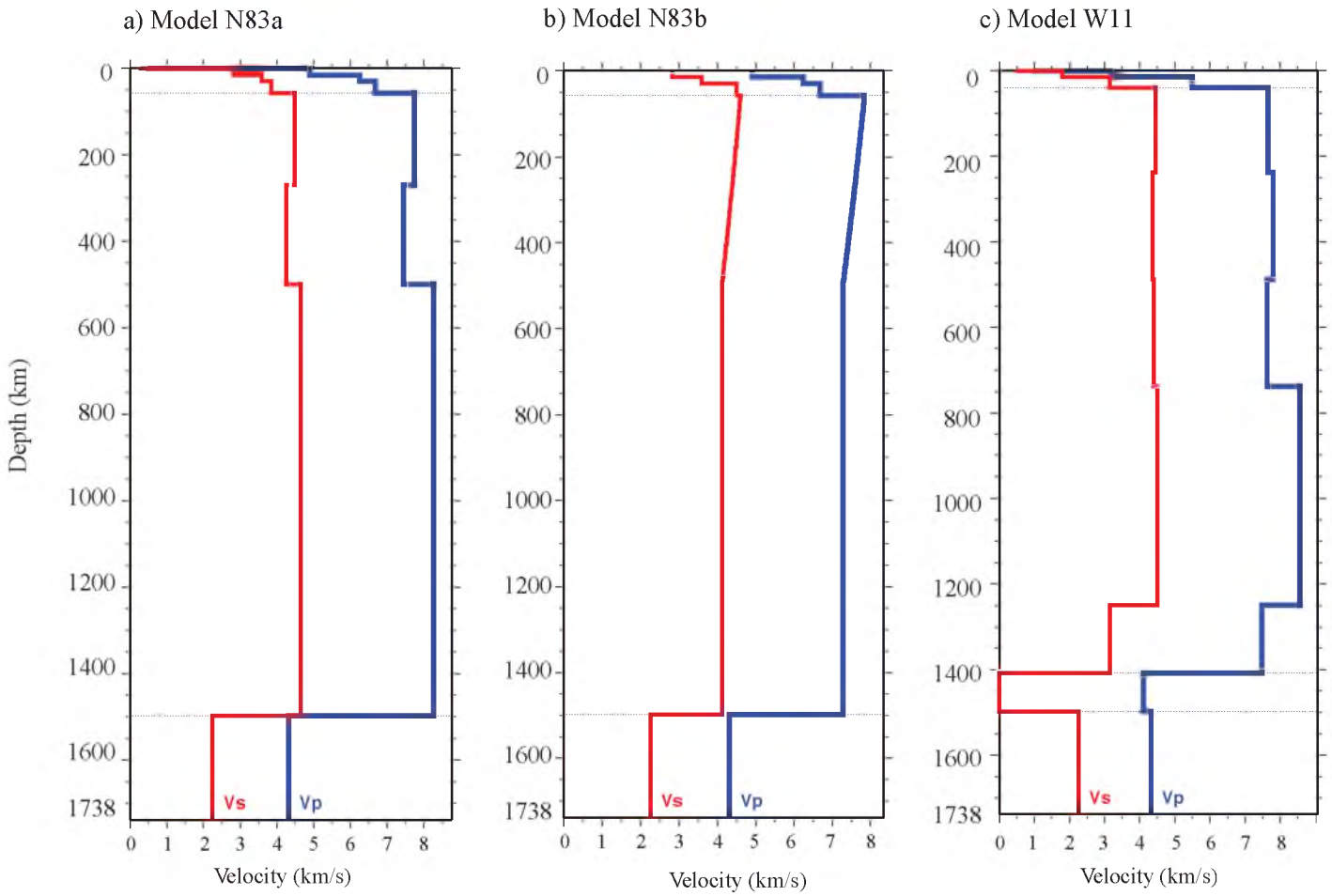

Figure 13. Shear wave and *P*-wave velocity structure for Model N83a, N83b, and W11. Core structure was adapted from Weber's work [*Weber et al.*, 2011].

Table 4. Model G81

Structure	Depth (km)	V_S (km/s)	V_P (km/s)	Density (g/cm3)	Quality Factor
Crust	0	2.96	5.1	3.33	5000
	20	3.9	6.8		
	60	4.57	7.75		
Upper Mantle	400	4.37	7.65		4000
Lower Mantle	480	4.2	7.6	3.66	1500
	1100	?	?		
Attenuating Zone	>1100				<500

Table 5. Model GB06

Depth (km)	V_S (km/s)	V_P (km/s)
1	0.5	0.8
11	1.8	3.5
28	4.37	7.65
38	4.44	7.65
238	4.37	7.79
448	4.37	7.62
487	4.4	7.62
738	4.5	8.15

Table 6. Model GG11

Depth (km)	V_S (km/s)	V_P (km/s)	Density (g/cm^3)
0.4	0.5	1	2.6
1.4	0.5	1	2.6
12.4	1.8	3.2	2.762
28.4	3.3	5.5	2.762
40.4	4.34	7.55	3.314
65.8	4.35	7.57	3.318
90.4	4.36	7.59	3.322
110.4	4.37	7.61	3.325
130.4	4.38	7.63	3.329
150.4	4.39	7.64	3.332
170.4	4.4	7.66	3.335
190.4	4.4	7.68	3.338
210.4	4.41	7.69	3.341
235.5	4.42	7.71	3.344
250.4	4.43	7.72	3.346
275.8	4.44	7.74	3.35
290.4	4.44	7.75	3.352
310.4	4.45	7.77	3.355
330.4	4.45	7.78	3.357
350.4	4.46	7.8	3.36
370.4	4.47	7.81	3.363
390.4	4.47	7.82	3.365
410.4	4.48	7.84	3.368
430.4	4.49	7.85	3.37
450.4	4.49	7.86	3.373
470.4	4.5	7.88	3.375
485.5	4.5	7.88	3.377
505.8	4.51	7.9	3.379
530.4	4.51	7.91	3.382
550.4	4.52	7.92	3.384
570.4	4.53	7.94	3.386
590.4	4.53	7.95	3.388
610.4	4.54	7.96	3.391
630.4	4.54	7.97	3.393
650.4	4.54	7.98	3.395

Table 6. *Continued*

Depth (km)	V_S (km/s)	V_P (km/s)	Density (g/cm^3)
670.4	4.55	7.99	3.397
690.4	4.55	8	3.398
710.4	4.56	8.01	3.4
735.5	4.56	8.02	3.403
750.4	4.57	8.03	3.404
775.8	4.57	8.04	3.406
790.4	4.57	8.05	3.408
810.4	4.58	8.06	3.409
830.4	4.58	8.07	3.411
850.4	4.58	8.08	3.413
870.4	4.59	8.08	3.414
890.4	4.59	8.09	3.416
910.4	4.59	8.1	3.417
930.4	4.6	8.11	3.419
950.4	4.6	8.12	3.42
970.4	4.6	8.12	3.421
990.4	4.61	8.13	3.423
1010.4	4.61	8.14	3.424
1030.4	4.61	8.14	3.425
1050.4	4.61	8.15	3.427
1070.4	4.62	8.16	3.428
1090.4	4.62	8.16	3.429
1110.4	4.62	8.17	3.43
1130.4	4.62	8.18	3.431
1150.4	4.62	8.18	3.433
1170.4	4.63	8.19	3.434
1190.4	4.63	8.19	3.435
1210.4	4.63	8.2	3.436
1230.4	4.63	8.2	3.437
1250.4	4.63	8.21	3.438
1270.4	4.63	8.21	3.438
1290.4	4.63	8.22	3.439
1310.4	4.64	8.22	3.44
1330.4	4.64	8.23	3.441
1350.4	4.64	8.23	3.442
1357.5	4.64	8.23	3.442

Table 7. Model KM02

Depth (km)	V_S (km/s)	V_P (km/s)
0	0	0
1	3.0	5.5
15	3.1	5.5
29	3.4	7
37	3.75	7
40	3.85	7.5
160	4.0	8
185	4.3	8
195	4.1	8
325	4.02	8
512	4.5	9.25
560	5.4	8.3
575	5.79	8.3
600	5.82	10
630	5.5	8.4
650	5.35	8.45
700	5.75	10.4
800	5.91	11.5
900	5.97	11.6
925	6.05	11.7
1000	6.09	12.3
1025	5.9	12.3
1137	5.8	9.7

Table 8. Model L03

Depth (km)	V_S (km/s)	V_P (km/s)
0	0.5	3.0
1	1.5	3.25
13	2.1	5.5
28	4.3	7.5
43	4.5	7.75
238	4.25	7.5
488	4.55	8.3
737	4.45	8.15

Table 9. Model N76

Structure	Depth (km)	V_S (km/s)	V_P (km/s)
Crust	0	3.4	4.5
	29	4.0	6.5
	30	4.7	8.14
	58	4.4	7.9
Upper Mantle	300	4.15	7.88
Middle Mantle	400	3.67	7.8
	800		
	>800	?	?

Table 10. Model N83a

Structure	Depth (km)	V_S (km/s)	V_P (km/s)
Crust	0	0.29*	0.51
	1	2.82*	4.90
	15	3.59*	6.25
	30	3.84*	6.68
	58	4.49	7.74
Mantle	270	4.25	7.46
	500	4.65	8.26
	1000	4.65	8.26
	>1000	?	?

*S-wave velocities were determined by dividing the P-wave velocity by 1.739.

Table 11. Model N83b

Structure	Depth (km)	V_S (km/s)	V_P (km/s)
Crust	0	0.29*	0.51
	1	2.82*	4.90
	15	3.59*	6.25
	30	3.84*	6.68
	58	4.49	7.74
Mantle	270	$0.302r^{0.367}$	$1.271r^{0.245}$
	500	4.65	8.26

*S-wave velocities were determined by dividing the P-wave velocity by 1.739. r, the radius of moon.

Table 12. Model W11

Structure	Depth (km)	V_S (km/s)	V_P (km/s)	Density (g/cm3)
	0.0	0.50	1.00	2.60
	1.0	1.80	3.20	2.70
	15.0	3.15	5.50	2.84
	40.0	4.44	7.65	3.33
	238.0	4.37	7.79	3.37
	488.0	4.40	7.62	3.37
	738.0	4.50	8.56	3.42
	1257.1	3.15	7.48	3.42
Outer-core	1407.1	0.00	4.11	5.10
Inner-core	1497.1	2.25	4.32	8.00

Table 13. Mean Squared Error of ten models. *

		G81	GB06	GG11	KM02	L03	N76	N83a	N83b	W11	YY13
P	A	5.7	23.5	3.2	6.7	4.1	5.5	3.6	5.5	4.6	3.8
	M	7.4	24.1	6.1	32.7	6.7	9.5	6.0	10.0	6.0	5.9
	S	15.5	27.3	14.3	34.2	12.8	16.4	13.7	17.7	15.0	14.5
	D	5.7	12.3	4.8	30.7	5.4	5.1	5.1	9.9	4.7	4.9
S	A	10.6	41.0	3.3	11.0	9.4	9.3	4.5	9.8	7.9	3.6
	M	13.0	42.0	10.5	20.2	12.8	13.7	9.2	14.2	12.2	8.8
	S	23.9	41.4	22.0	36.5	22.4	24.2	22.5	24.7	23.8	22.5
	D	12.5	20.0	13.5	33.8	11.6	27.2	13.9	14.3	11.5	12.0
S-P	A	2.9	17.9	1.7	2.5	11.5	4.7	0.8	2.8	4.6	1.8
	M	12.1	21.2	11.7	30.3	15.1	10.9	10.7	12.8	12.1	11.1
	S	17.1	17.6	13.9	38.6	16.6	14.4	14.1	16.3	12.9	13.8
	D	9.7	12.0	8.8	26.6	11.2	32.6	8.7	16.9	13.4	9.2
All		11.4	21.0	10.8	30.6	11.4	23.3	10.8	15.5	11.0	10.6

* P, S, and S-P means P-wave, S-wave and S-P differential travel time mean squared error calculation.
A = Artificial Impacts.
M = Meteoroid Impacts.
S = Shallow Moonquakes.
D = Deep moonquakes.

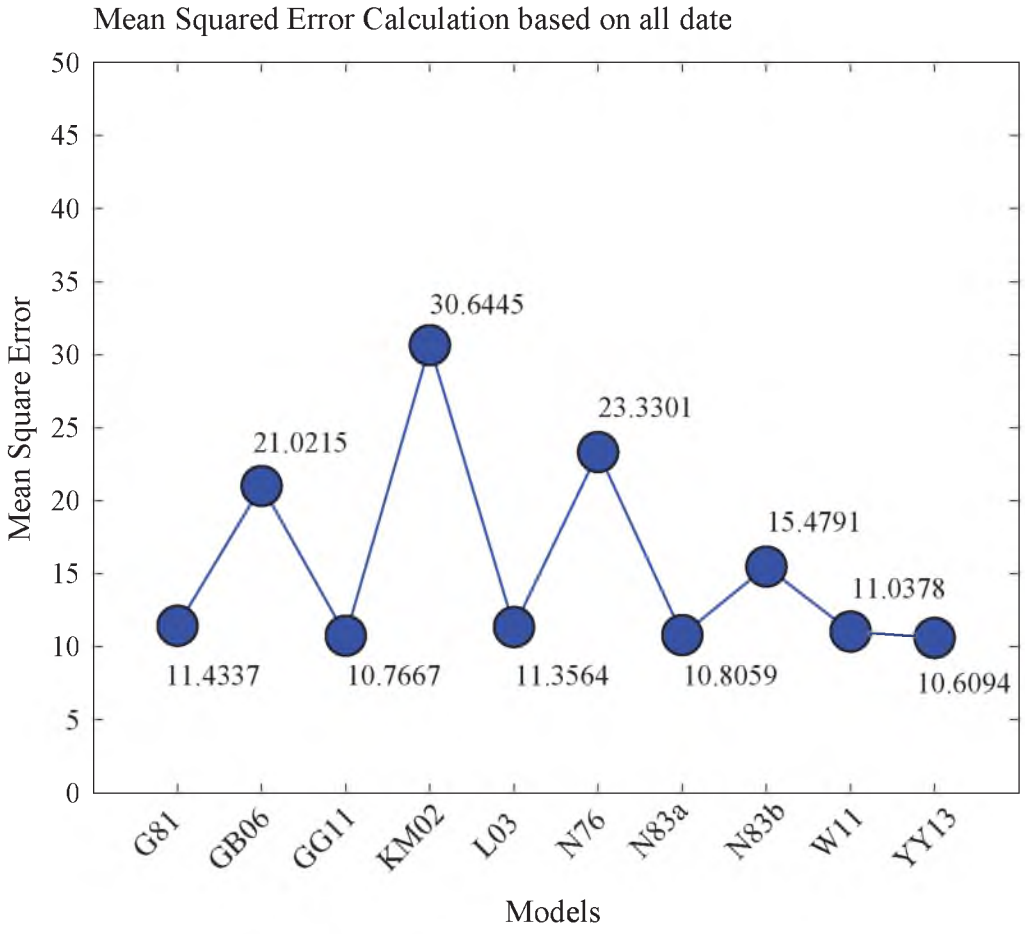

Figure 14. Mean squared error calculated based on all the data. YY13 has the smallest error along a total of 10 lunar seismic velocity models. Values of mean squared error for each model were shown beside the points.

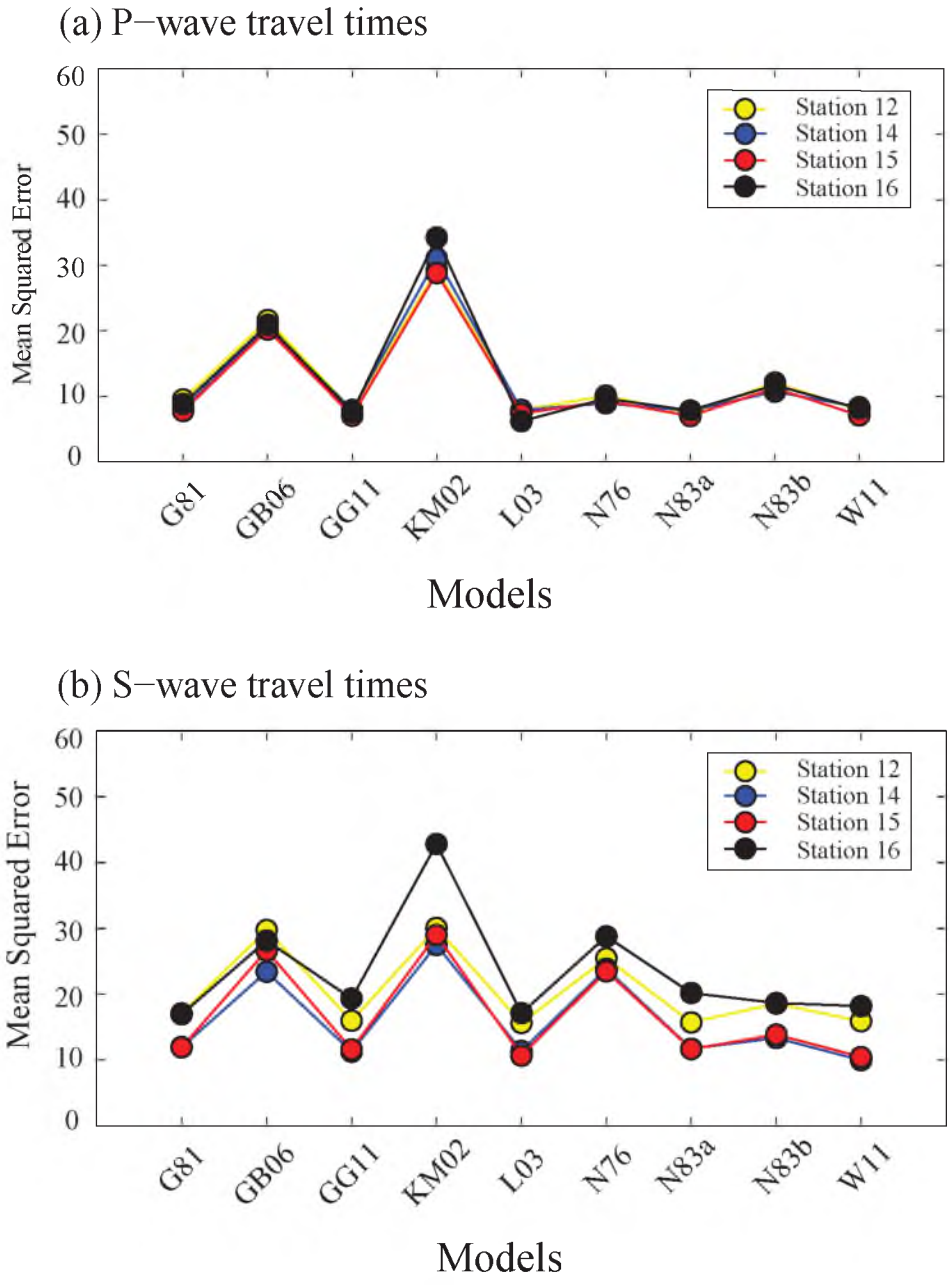

Figure 15. Mean squared error calculated based on four stations. For *P*-wave, significant difference was not available. However, for *S*-wave, Station 16 has a relatively higher error than other stations, which is consistent with the conclusion that seismograms recorded at station 16 were more scattering.

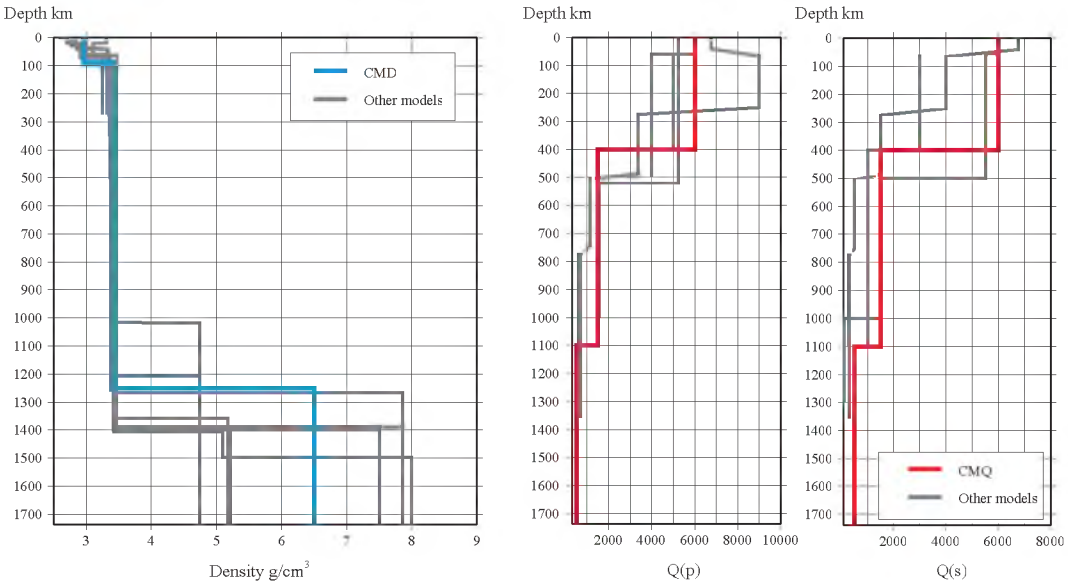

Table. 1 Common density model (CMD)

Depth km	Density g/cm
0	2.95
86	3.41
1250	6.5
1738	6.5

Table. 2 Common quality factor model (CMQ)

Depth km	Q(p)	Q(s)
0	6000	6000
400	1500	1500
1100	500	500
1738	500	500

Figure 16. Average density and Q factor model used in generating synthetic seismograms.

REFERENCES

Berckhemer, H. (1970), A possible scattering mechanism for lunar seismic waves, *Zeitschrift fur Geophysik*, *36*, 523-529.

Bills, B. G., and A. J. Ferrari (1977), A lunar density model consistent with topographic, gravitational, librational, and seismic data, *Journal of Geophysical Research*, *82*(8), 1306-1314.

Bulow, R., C. Johnson, and P. Shearer (2005), New events discovered in the Apollo lunar seismic data, *J. geophys. Res*, *110*(10).

Cooper, M. R., R. L. Kovach, and J. S. Watkins (1974), Lunar near-surface structure, *Reviews of Geophysics*, *12*(3), 291-308.

Crotwell, H. P., T. J. Owens, and J. Ritsema (1999), The TauP Toolkit: Flexible seismic travel-time and ray-path utilities, *Seismological Research Letters*, *70*, 7.

Dainty, A. M., M. N. Toksöz, K. R. Anderson, P. J. Pines, Y. Nakamura, and G. Latham (1974), Seismic scattering and shallow structure of the Moon in Oceanus Procellarum, *Earth, Moon, and Planets*, *9*(1), 11-29.

Friederich, W., and J. Dalkolmo (1995), Complete synthetic seismograms for a spherically symmetric earth by a numerical computation of the Green's function in the frequency domain, *Geophysical Journal International*, *122*(2), 537-550.

Frohlich, C., and Y. Nakamura (2006), Possible extra-Solar-System cause for certain lunar seismic events, *Icarus*, *185*(1), 21-28.

Gagnepain-Beyneix, J., P. Lognonnè, H. Chenet, D. Lombardi, and T. Spohn (2006), A seismic model of the lunar mantle and constraints on temperature and mineralogy, *Physics of the Earth and Planetary Interiors*, *159*(3-4), 140-166.

Garcia, R. F., J. Gagnepain-Beyneix, S. Chevrot, and P. Lognonnè (2011), Very preliminary reference Moon model, *Physics of the Earth and Planetary Interiors*.

Goins, N. (1978), Lunar seismology: The internal structure of the Moon, *Ph.D. thesis, Mass. Inst. of Technol., Cambridge*.

Goins, N., A. Dainty, and M. Toksöz (1981), Lunar seismology: The internal structure of the Moon, *Journal of Geophysical Research*, *86*(B6), 5061-5074.

Gold, T., and S. Soter (1970), Apollo 12 seismic signal: Indication of a deep layer of powder, *Science*, *169*(3950), 1071-1075.

Hood, L., and J. Jones (1987), Geophysical constraints on lunar bulk composition and structure: a reassessment, *Journal of Geophysical Research*, *92*(B4), E396-E410.

Khan, A., and K. Mosegaard (2002), An inquiry into the lunar interior: A nonlinear inversion of the Apollo lunar seismic data, *J. geophys. Res*, *107*(E6), 19-44.

Kuskov, O. (1997), Constitution of the Moon: 4. Composition of the mantle from seismic data, *Physics of the Earth and Planetary Interiors*, *102*(3-4), 239-257.

Kuskov, O., and V. Kronrod (1998), Constitution of the Moon:: 5. Constraints on composition, density, temperature, and radius of a core, *Physics of the Earth and Planetary Interiors*, *107*(4), 285-306.

Latham, M. Ewing, F. Press, and G. Sutton (1969), The Apollo passive seismic experiment, *Science*, *165*(3890), 241-250.

Latham, G., M. Ewing, F. Press, G. Sutton, J. Dorman, Y. Nakamura, N. Toks6z, F. Duennebier, and D. Lammlein (1971), Apollo 14 Preliminary Science Report, edited, NASA SP-272.

Lognonnè, P., J. Gagnepain-Beyneix, and H. Chenet (2003), A new seismic model of the Moon: implications for structure, thermal evolution and formation of the Moon, *Earth and Planetary Science Letters*, *211*(1-2), 27-44.

Lognonné, P., and C. Johnson (2007), 10.03 - Planetary Seismology, in *Treatise on Geophysics*, edited by G. Schubert, pp. 69-122, Elsevier, Amsterdam, doi:10.1016/b978-044452748-6.00154-1.

Nakamura, Y. (1983), Seismic velocity structure of the lunar mantle, *Journal of Geophysical Research*, *88*(B1), 677-686.

Nakamura, Y. (2003), New identification of deep moonquakes in the Apollo lunar seismic data, *Physics of the Earth and Planetary Interiors*, *139*(3), 197-205.
Nakamura, Y. (2005), Farside deep moonquakes and deep interior of the Moon, *Journal of Geophysical Research*, *110*(E1), E01001.

Nakamura, Y., F. K. Duennebier, G. V. Latham, and H. J. Dorman (1976), Structure of the lunar mantle, *Journal of Geophysical Research*, *81*(26), 4818-4824.

Nakamura, Y., G. V. Latham, and H. J. Dorman (1982), Apollo lunar seismic experiment-final summary.

Schmitt, J., G. Heiken, D. Vaniman, and B. M. French (1991), *Lunar sourcebook: A user's guide to the Moon*, Cambridge University Press.

Toksöz, M. N., A. M. Dainty, S. C. Solomon, and K. R. Anderson (1974), Structure of the Moon, *Reviews of Geophysics*, *12*(4), 539-567.

Weber, R. C., P. Y. Lin, E. J. Garnero, Q. Williams, and P. Lognonne (2011), Seismic detection of the lunar core, *Science*, *331*(6015), 309.